The Astrophysical Journal, 985:72 (14pp), 2025 May 20 https://doi.org/10.3847/1538-4357/adc91d
© 2025. The Author(s). Published by the American Astronomical Society.
OPEN ACCESS

XUE: Thermochemical Modeling Suggests a Compact and Gas-depleted Structure for a Distant, Irradiated Protoplanetary Disk

Bayron Portilla-Revelo[1,2], Konstantin V. Getman[1], María Claudia Ramírez-Tannus[3], Thomas J. Haworth[4], Rens Waters[5,6], Arjan Bik[7], Eric D. Feigelson[1,8], Inga Kamp[9], Sierk E. van Terwisga[10], Jenny Frediani[7], Thomas Henning[3], Andrew J. Winter[3,11], Veronica Roccatagliata[12,13], Thomas Preibisch[14], E. Sabbi[15], Peter Zeidler[16], and Michael A. Kuhn[17]

[1] Department of Astronomy and Astrophysics, The Pennsylvania State University, 525 Davey Laboratory, University Park, PA 16802, USA; bmp5924@psu.edu
[2] Center for Exoplanets and Habitable Worlds, Penn State University, 525 Davey Laboratory, 251 Pollock Road, University Park, PA 16802, USA
[3] Max-Planck Institut für Astronomie (MPIA), Königstuhl 17, D-69117 Heidelberg, Germany
[4] Astronomy Unit, School of Physics and Astronomy, Queen Mary University of London, London, E1 4NS, UK
[5] Department of Astrophysics/IMAPP, Radboud University, PO Box 9010, 6500 GL Nijmegen, The Netherlands
[6] SRON Netherlands Institute for Space Research, Niels Bohrweg 4, NL-2333 CA Leiden, The Netherlands
[7] Department of Astronomy, Stockholm University, AlbaNova University Center, SE-10691 Stockholm, Sweden
[8] Center for Astrostatistics, Pennsylvania State University, 517 Thomas Building, University Park, PA 16802, USA
[9] Kapteyn Astronomical Institute, University of Groningen, PO BOX 800, 9700 AV Groningen, The Netherlands
[10] Space Research Institute, Austrian Academy of Sciences, Schmiedlstr. 6, 8042, Graz, Austria
[11] Université Côte d'Azur, Observatoire de la Côte d'Azur, CNRS, Laboratoire Lagrange, 06300 Nice, France
[12] Dipartimento di Fisica e Astronomia, Alma Mater Studiorum, Universitàdi Bologna, Via Gobetti 93/2, I-40129 Bologna, Italy
[13] INAF-Osservatorio Astrofisico di Arcetri, Largo E. Fermi 5, I-50125 Firenze, Italy
[14] Universitäts-Sternwarte München, Ludwig-Maximilians-Universität, Scheinerstr. 1, 81679 München, Germany
[15] Gemini Observatory/NSFs NOIRLab, 950 N. Cherry Avenue, Tucson, AZ 85719, USA
[16] AURA for the European Space Agency (ESA), ESA Office, Space Telescope Science Institute, 3700 San Martin Drive, Baltimore, MD 21218, USA
[17] Centre for Astrophysics Research, Department of Physics, Astronomy and Mathematics, University of Hertfordshire, Hatfield, AL10 9AB, UK
Received 2024 December 16; revised 2025 March 14; accepted 2025 March 28; published 2025 May 20

Abstract

Unveiling the physical structure of protoplanetary disks is crucial for interpreting the diversity of the exoplanet population. Until recently, the census of the physical properties of protoplanetary disks probed by mid-infrared observations was limited to the solar neighborhood ($d \lesssim 250$ pc). However, nearby star-forming regions (SFRs) such as Taurus—where no O-type stars reside—are not representative of the environments where the majority of the planet formation occurs in the Galaxy. The James Webb Space Telescope (JWST) now enables observations of disks in distant high-mass SFRs, where strong external far-ultraviolet radiation is expected to impact those disks. Nevertheless, a detailed characterization of the population of externally irradiated disks is still lacking. We use the thermochemical code `ProDiMo` to model JWST/MIRI spectroscopy and archival visual/near-infrared photometry aiming to constrain the physical structure of the irradiated disk around the solar-mass star XUE 1 in NGC 6357 ($d \approx 1690$ pc). Our findings are as follows. (1) Mid-infrared dust emission features are explained by amorphous and crystalline silicates with compositions similar to nearby disks. (2) The molecular features detected with MIRI originate within the first ~1 au, consistent with results from slab models. (3) Our model favors a disk truncated at 10 au with a gas-to-dust ratio of unity in the outskirts. (4) Comparing models of the same disk structure under different irradiation levels, we find that strong external irradiation raises gas temperature tenfold and boosts water abundance beyond 10 au by a factor of 100.

Unified Astronomy Thesaurus concepts: Star forming regions (1565); Planet formation (1241); Protoplanetary disks (1300); Infrared spectroscopy (2285); Radiative transfer simulations (1967)

1. Introduction

Protoplanetary disks are a by-product of the stellar formation process and are commonly observed during the first several million years of stellar evolution (A. J. W. Richert et al. 2018; C. F. Manara et al. 2023). The most fundamental properties of a disk—its size, the amount of dust and gas, and its chemical composition—will determine the conditions for planet formation within the disk (C. Mordasini et al. 2012). Such properties can be altered by external environmental conditions. Three major effects capable of shaping disk evolution that are set by the environment are star–disk gravitational interactions (e.g., K. Vincke & S. Pfalzner 2018), late stage infall of material from the parent cloud (e.g., P. Padoan et al. 2005; M. Kuffmeier et al. 2023; A. J. Winter et al. 2024), and external photoevaporation driven by far-ultraviolet (FUV) photons (e.g., D. Johnstone et al. 1998). This work focuses on the latter effect.

Just as OB stars produce ionized H II regions in their natal molecular clouds, they will ionize and photoevaporate the protoplanetary disks of nearby low-mass stars. The external FUV flux measured at a disk's surface scales with the number density of OB stars in the field, which positively correlates with the total number of members in the star-forming region (SFR; A. J. Winter & T. J. Haworth 2022). This implies that disks formed in high-mass SFRs overall experience a substantially higher FUV flux compared to those in low-mass SFRs. Given that at least 50% of stars and planetary systems form in such

Original content from this work may be used under the terms of the Creative Commons Attribution 4.0 licence. Any further distribution of this work must maintain attribution to the author(s) and the title of the work, journal citation and DOI.

massive regions (e.g., M. R. Krumholz et al. 2019), it follows that planet formation predominantly occurs in environments with strong external FUV fields.

The effect of a strong FUV field on a disk is twofold: it affects the disk's surface density (e.g., P. J. Armitage 2020), and it alters the disk's chemistry (see, e.g., F. C. Adams 2010 for a discussion on the chemical signatures of strong radiation fields in forming planetary systems, and S. Desch & N. Miret-Roig 2024 on the implications for meteoritics). External photoevaporative winds enhance the rate of gas mass loss leading to an accelerated shrinkage of the disk radius (T. J. Haworth et al. 2018; G. A. L. Coleman & T. J. Haworth 2022; A. J. Winter & T. J. Haworth 2022). External photoevaporation can also influence the distribution of solids, particularly that of submicron-sized grains—which are well coupled to the gas—which will be carried away by the wind (S. Facchini et al. 2016; A. D. Sellek et al. 2020; A. J. Winter & T. J. Haworth 2022). Overall, an accelerated gas mass-loss rate will reduce the mass budget and the time available for planet formation and migration (A. J. Winter & T. J. Haworth 2022; L. Qiao et al. 2023; S. Huang et al. 2024). On the other hand, external FUV radiation is expected to substantially increase the temperature at intermediate and surface layers (B. Ercolano & G. Picogna 2022). A high flux of FUV photons is also expected to cause a different chemical stratification in the disk, leading to significant differences in both the abundance of certain molecular species and their observational signatures, compared to those in nonirradiated disks (C. Walsh et al. 2013; S. Antonellini et al. 2015; L. Keyte & T. J. Haworth 2025).

The Orion Molecular Cloud Complex has been one suitable testbed for these theoretical predictions. Since the first observation of irradiated disks (C. R. O'Dell et al. 1993), multiple works have targeted different subregions in the Orion Complex. These studies have allowed us to constrain the time span that some disks have been exposed to UV radiation (J. Bally et al. 1998; C. J. Clarke 2007), establish that inner disks around YSO's can survive even in the presence of neighboring ionizing stars (A. J. W. Richert et al. 2015), find evidence for disk mass gradients relative to the distance to the ionizing sources (S. E. van Terwisga et al. 2019; S. E. van Terwisga & A. Hacar 2023), and compare the cold gas-phase chemistry between irradiated and nonirradiated disks (J. K. Díaz-Berríos et al. 2024).

More recently, the James Webb Space Telescope (JWST) has observed disks in the Orion Nebula region. O. Berné et al. (2023) reported the first detection of CH_3^+—a key molecule in gas-phase organic chemistry—in the outskirts of the irradiated protoplanetary disk d203-506 (see also M. Zannese et al. 2025). The physical structure of this disk was later characterized by O. Berné et al. (2024) through modeling of observed near-IR H_2 emission lines. M. Zannese et al. (2024) conducted a combined near- and mid-infrared spectroscopic study of OH in the same disk, revealing a "warm water cycle" in which H_2O is efficiently destroyed and reformed under FUV radiation. Finally, J. R. Goicoechea et al. (2024) reported near-IR C I fluorescent emission, triggered by FUV pumping, tracing both the disk's upper layers and the photoevaporative wind.

These findings underscore the importance of studying disks in irradiated environments. However, one distinctive feature of the Orion Nebular Cluster is that a single, centrally localized star—θ^1 Ori C—is already responsible for ∼80% of the H-ionizing photons. Another region of interest is the OB association IC 1795. Synergistic X-ray and infrared observations allowed for the determination of both the spatial distribution of disks and the disk fraction dependence on the stellar mass (V. Roccatagliata et al. 2011). IC 1795 hosts only two O-type stars once more.

The advent of the JWST has opened a new window in the study of irradiated disks. Its enhanced sensitivity and resolution allow us to study disks in high-mass SFRs at kiloparsec-distance scales. One of those regions is NGC 6357 ($d \approx 1690$ pc). This region hosts some of the most massive O2 and O3 stars known in the Galaxy (N. R. Walborn 2003), along with an additional 20 O-type stars (D. Russeil et al. 2010; P. S. Broos et al. 2013; M. S. Povich et al. 2013; M. C. Ramírez-Tannus et al. 2020). The eXtreme Ultraviolet Environments (XUE) program (GO 1759; M. C. Ramirez-Tannus et al. 2021) targeted 12 disks in NGC 6357 with the MIRI/MRS instrument. For those disks, the strength of the external FUV field ranges from 10^3 to 10^6 times the value in the solar neighborhood. M. C. Ramírez-Tannus et al. (2023) performs the initial characterization of one of those sources—the disk around the T Tauri star XUE 1. Using a slab-modeling approach, they report the presence of CO, H_2O, C_2H_2, HCN, and CO_2. Their retrieval approach suggests that the properties of those molecular tracers (emitting areas, column densities, and excitation temperatures) are indistinguishable from those observed in nearby, nonirradiated disks.

While slab models are pivotal in the initial characterization of a disk, an in-depth understanding of its structure requires increasing modeling complexity. This next level of complexity materializes as thermochemical models, which are also crucial to inform future observational campaigns focusing on probing different physical conditions in the disk (I. Kamp 2015; I. Kamp et al. 2023). We introduce the first thermochemical model, driven by JWST/MIRI and archival data, of a protoplanetary disk that is constantly exposed to an FUV field 10^5 times stronger than the solar neighborhood value. Based on this model, we aim to constrain the physical structure of the XUE 1 disk.

Section 2 introduces the data set used in this study as well as the modeling approach. Section 3 presents our constraints on the dust and gas distributions as well as the inferred gas temperature and molecular abundances of selected species that we obtain from the model that best explains the data. These results are contrasted to what would be expected if the disk were irradiated with a weaker FUV field. In Section 4, we compare our results to those from slab models, elaborate on the key assumptions of our thermochemical model, and relate our findings to the predictions from radiation-hydrodynamical models of photoevaporated disks. We present our conclusions in Section 5.

2. Observations and Methods

2.1. Stellar Properties

XUE 1 is a stellar member of the rich young stellar cluster Pismis 24, situated within the massive SFR NGC 6357. The projected distances from XUE 1 to the most luminous nearby O-type stars range from 0.3 to 0.5 pc (Figure 1).

Based on the Chandra X-ray and near-infrared (NIR) 2MASS and UKIRT JHK_s data, combined with the theoretical predictions from the pre-main-sequence (PMS) PARSEC 1.2S evolutionary model (A. Bressan et al. 2012; Y. Chen et al. 2014),

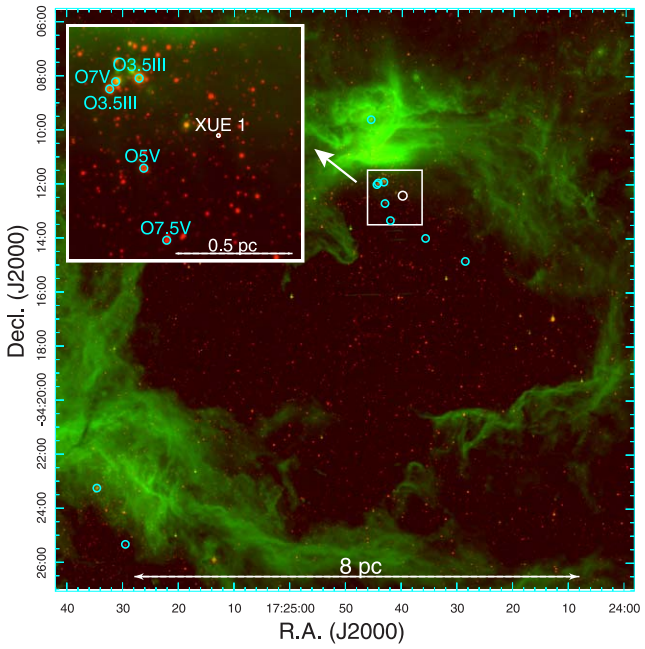

Figure 1. Composite image of the CS 61 bubble in the NGC 6357 star-forming region, covering 20 × 20 arcmin^2 and combining UKIRT K_s-band (red) with Spitzer-IRAC 8.0 μm (green) data. The bubble hosts the rich Pismis 24 young stellar cluster. The K_s-band highlights the stellar component, including both members of the Pismis 24 cluster and unrelated field stars, while the 8.0 μm band reveals warm dust from the parental cloud, heated by intense radiation from massive stars. XUE 1 and known ionizing O-type stars are marked with white and cyan circles, respectively. Inset: a 2 × 2 arcmin^2 close-up of the XUE 1 neighborhood, with spectral types of the nearest O-type stars labeled.

K. V. Getman & E. D. Feigelson (2021) and K. V. Getman et al. (2022) derive stellar properties for numerous young stellar members of over 40 nearby Galactic SFRs, including NGC 6357. These stellar properties include time-averaged X-ray luminosities, approximate stellar ages, source extinctions, effective temperatures, bolometric luminosities, and masses.

XUE 1 is the primary component (A1) in a binary stellar system A1+A2, with a component separation of 0.″2 (∼300 au). The binary remains unresolved in Spitzer mid-infrared (MIR), UKIRT, and VISTA NIR images, as well as Chandra X-ray images (P. S. Broos et al. 2013; R. R. King et al. 2013; M. S. Povich et al. 2013; L. K. Townsley et al. 2019). However, the XUE 1 stellar component is resolved in the archived optical HST ACS and our JWST/MIRI MIR images.

Assuming a total-to-selective extinction factor of $R_V = 3.3$ for NGC 6357 (F. Massi et al. 2015; D. Russeil et al. 2017; M. Fouesneau et al. 2022) and using the extinction law from K. D. Gordon et al. (2023; see also M. Decleir et al. 2022; E. L. Fitzpatrick et al. 2019; K. D. Gordon et al. 2009, 2021), the binary system's NIR-based extinction was inferred to be $A_V = 9.2$ mag, with an estimated age of ∼0.7 Myr (K. V. Getman et al. 2022). These values are consistent with those of numerous nearby young stellar members of NGC 6357. Further assuming that the HST z-band magnitudes of the binary components are unaffected by accretion, and using the PARSEC 1.2S model along with the aforementioned source extinction and stellar age values, we derive stellar masses of 1.2 and 0.7 $M_\odot$ for the A1 (XUE 1) and A2 stellar components, respectively. The PARSEC-based stellar bolometric luminosity and effective temperature for XUE 1 are 3.9 $L_\odot$ and 4729 K, respectively.

The X-ray luminosity and column density measurements independently confirm the inferred mass of XUE 1. The X-ray luminosity of the whole binary system, $\log(L_X) = 30.4$ erg s^{-1}, is dominated by XUE 1 (L. K. Townsley et al. 2019). This X-ray value is consistent with the stellar mass of ∼1 $M_\odot$ according to the well-known empirical PMS L_X–M correlation (T. Preibisch et al. 2005; A. Telleschi et al. 2007). The gas column density of $\log(N_H) = 22.2$ cm^{-2} is also in line with the dust visual extinction value, assuming the typical gas-to-dust ratio $N_H/A_V = 2 \times 10^{21}$ cm^{-2} (H. Zhu et al. 2017).

2.2. Protoplanetary Disk Data

2.2.1. JWST/MIRI Spectroscopy

We summarize the main results from the JWST/MIRI/MRS observations of XUE 1 that will inform our modeling. For a detailed description of the data acquisition and analysis, refer to M. C. Ramírez-Tannus et al. (2023).

In this work, we use an updated reduction of the MIRI spectrum obtained with JWST Pipeline version 1.14.0. This new reduction achieves a signal-to-noise ratio of 110 and a noise level of $\sigma = 0.12$ mJy. We measure these values in the line-free interval $15.865 < \lambda < 15.952$ μm. Our MIRI-MRS observations achieve an angular resolution at 7 μm of ∼0.″35 (D. R. Law et al. 2023), which translates into ∼600 au at the distance of NGC 6357. We deredden the spectrum using a total-to-selective extinction factor $R_V = 3.3$, a visual extinction of $A_V = 9.2$ mag (Section 2.1), and the K. D. Gordon et al. (2023) extinction law. A visual inspection of the underlying continuum already confirms the presence of amorphous and crystalline silicates (we elaborate on the continuum characterization in Section 2.3.1).

Line emission features in both MIRI channels 1 ($4.90 \leqslant \lambda \leqslant 7.65$ μm) and 3 ($11.55 \leqslant \lambda \leqslant 17.98$ μm) match their respective counterparts as seen in version 1.9.4 of the data reduction (M. C. Ramírez-Tannus et al. 2023). Thus, we confirm the presence of HCN, H_2O, C_2H_2, CO_2, and CO. In addition to those features, our new reduction also displays a weak signal from OH (∼1 mJy flux level) at ∼16.0 μm and ∼16.8 μm. These lines are pure rotational transitions of the ground electronic state and their quantum numbers are (0, 18.5, 1, f) → (0, 17.5, 1, f) and (0, 16.5, 2, e) → (0, 15.5, 2, e), respectively.[18]

2.2.2. Archival Photometry

We use archival optical and NIR data from HST, VISTA and Spitzer. From these data, only HST is capable of resolving XUE 1 from the binary pair; accordingly, we adopt VISTA and Spitzer data as lower limits for the apparent magnitude of XUE 1.

We correct for extinction in the same way as for the MIRI data. Zero-points and reference wavelengths for each filter are taken from the SVO Filter Profile Service (C. Rodrigo et al. 2012; C. Rodrigo & E. Solano 2020). We summarize the photometry toward the source in Table 1.

[18] Notation follows J. S. A. Brooke et al. (2016). A quantum state is written as (v, J, F, p), where v indicates the vibrational level, J is the total angular momentum quantum number, F indicates the hyperfine state, and p is the parity of the Λ-doubling state.

Table 1
Compilation of Astrometric and Photometric Data toward XUE 1

R.A.	$17^h24^m40^s.100$
Decl.	$-34^d12^m25^s.36$
Distance	1690 pc
Photometric Properties	

Instrument	Magnitude	Extinction-corrected flux (erg s^{-1} cm^{-2} Å^{-1})
HST/ACS—550M	$V = 22.7$	1.03×10^{-14}
- 850LP	$z = 17.9$	3.26×10^{-15}
VISTA/NIR	$J \geqslant 15.07$	$\leqslant 3.31 \times 10^{-15}$
	$H \geqslant 12.99$	$\leqslant 3.18 \times 10^{-15}$
	$K_s \geqslant 12.80$	$\leqslant 8.51 \times 10^{-16}$
Spitzer/IRAC.I1	[3.6 μm] $\geqslant 10.56$	$\leqslant 5.96 \times 10^{-16}$
IRAC.I2	[4.5 μm] $\geqslant 10.27$	$\leqslant 2.81 \times 10^{-16}$
IRAC.I3	[5.8 μm] $\geqslant 9.84$	$\leqslant 1.56 \times 10^{-16}$
IRAC.I4	[8.0 μm] $\geqslant 9.24$	$\leqslant 8.19 \times 10^{-17}$

Note. Inequalities indicate lower (upper) limits on the magnitude (flux) from the unresolved A1 component.

2.3. Modeling

2.3.1. Continuum Estimation and Characterization

In the following analysis of the dust population characterization, we first calculate the dust continuum emission level from the MIRI spectrum using the `ctool` package (K. M. Pontoppidan et al. 2024), and then input this information into the Dust Continuum Kit (`DuCK`; H. Jang et al. 2024; T. Kaeufer et al. 2024) package to derive the dust composition.

We use the `ctool` package to estimate the underlying continuum in the $5 \leqslant \lambda \leqslant 28$ μm range of the MIRI spectrum. `ctool` estimates the continuum iteratively; it starts by median filtering the initial spectrum with a kernel size equal to `boxsize` wavelength channels. This filtering step produces a smoothed spectrum. The initial and smoothed spectra are compared to each other to generate a new continuum estimate: fluxes in the initial spectrum stronger than the smoothed flux are rejected and replaced by interpolating neighboring values `threshold` times weaker than the smoothed flux. These steps are repeated `niter` times, after which the remaining signal is convolved with a Savitzky–Golay filter. We run `ctool` using its default parameters: `niter=5`, `boxsize=95`, and `threshold=0.998`. As a preprocessing step, we first remove the broad molecular features using the slab models for C_2H_2, HCN, and CO_2 found by M. C. Ramírez-Tannus et al. (2023).

We perform a retrieval analysis to identify which dust species are shaping the continuum in the mid-IR; this will inform the thermochemical code about an appropriate set of dust opacities to use when solving the continuum radiative transfer. However, this work does not aim at a detailed study of the mineralogy in XUE 1.

We use the Dust Continuum Kit (`DuCK`) package. `DuCK` retrieves the grain composition in two steps. First, `DuCK` simulates the continuum emission as a linear combination of four flux terms: a star, an optically thick inner rim, an optically thick midplane, and an optically thin surface. In particular, the flux from the optically thin surface is modeled as the sum of individual terms over the number of dust species considered. Each individual term is proportional to the radial integral of a blackbody function weighted by the optical depth of the respective dust species.[19] In a second step, `DuCK` generates models for the total flux using multimodal nested sampling and determines the best-fit parameters, given an observation, by evaluating a likelihood function.

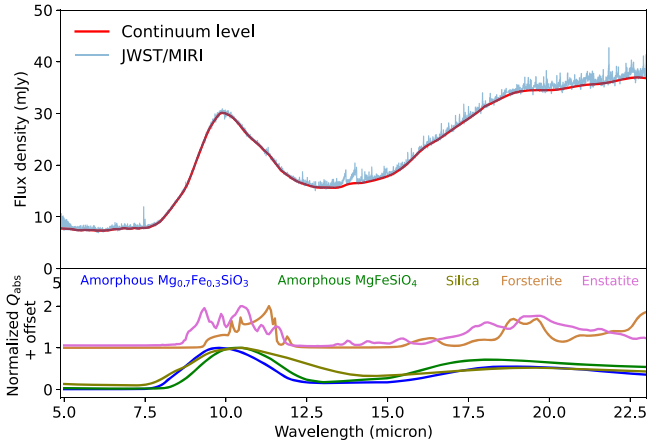

Figure 2. Characterization of the optically thin dust in the XUE 1 disk. Top: the blue curve is the total (dust+lines) JWST/MIRI spectrum and the red curve is the continuum level estimated with `ctool`. Bottom: absorption efficiency curves. The curves are for 1 μm pure grains whose composition is color-coded.

`DuCK` finds evidence for both amorphous and crystalline silicates.[20] In the amorphous category, we find silica (SiO_2) as well as amorphous silicates with SiO_3 stoichiometry ($Mg_{0.7}Fe_{0.3}SiO_3$) and SiO_4 stoichiometry ($MgFeSiO_4$). In the crystalline category, we find forsterite (Mg_2SiO_4) and crystalline $Mg_{0.96}Fe_{0.04}SiO_3$ (that we refer hereafter as enstatite). We do not find evidence for iron-rich minerals such as fayalite (Fe_2SiO_4) and troilite (FeS). The nondetection of troilite is expected given the absence of strong solid state resonances within the MIRI range. The estimated continuum level and the absorption efficiency curves of the retrieved species are shown in Figure 2.

2.3.2. Thermochemical Modeling

We use the `ProDiMo` code (P. Woitke et al. 2009; I. Kamp et al. 2010; W. F. Thi et al. 2011; P. Woitke et al. 2016; C. Rab et al. 2018; P. Woitke et al. 2024) to perform thermochemical modeling of the XUE 1 disk. `ProDiMo` is a radiation thermochemical code that self-consistently solves for the continuum radiative transfer, the gas heating–cooling balance and the chemistry in a protoplanetary disk. The code assumes a two-dimensional geometry implemented on a cylindrical grid (r, z), where r is the radial coordinate measured from the inner rim, and z is the vertical coordinate measured from the disk midplane. Simulations are carried out with `ProDiMo` version `V.3.0.0`, revision `9f058bf9` (P. Woitke et al. 2024). This is an improved and expanded version of the code that is capable to fit JWST spectra. Some of the new features include an improved escape probability algorithm to calculate line fluxes and emitting areas (P. Woitke et al. 2024), spectroscopic data for local thermodynamic equilibrium (LTE) calculations taken

[19] We use dust opacities computed with the Distribution of Hollow Spheres formalism (M. Min et al. 2005).
[20] Evidence for the presence of a species means that `DuCK` retrieves a total mass fraction higher than 1% for that species.

from HITRAN 2020 (I. E. Gordon et al. 2022) database, and the addition of new data for selected hydrocarbons (A. M. Arabhavi et al. 2024); an improved treatment for the calculation of UV photo-rates and molecular shielding factors (P. Woitke et al. 2024).

In light of the scarcity of data, we built on two working assumptions and a series of initial conditions. Our assumptions are based on either well-established observational results or theoretical grounds.

Assumption 1: XUE 1 is a primordial disk. We assume the disk has no substructures, and that the dust and gas distributions follow a continuous, exponentially decaying profile in the radial direction and a Gaussian profile in the vertical direction. The gas and dust surface densities can therefore be written as

$$\Sigma(r) = \Sigma_0 \left(\frac{R_{\rm tap}}{r}\right)^{\epsilon} \exp\left[-\left(\frac{r}{R_{\rm tap}}\right)^{2-\gamma}\right], \quad (1)$$

where the constant Σ_0 scales with the disk mass and $R_{\rm tap}$ is the tapering radius, i.e., the distance marking the transition from a linear to an exponential decay of the surface density profile. We assume a self-similar constraint on the exponents, setting $\epsilon = \gamma = 1$ (D. Lynden-Bell & J. E. Pringle 1974; A. M. Hughes et al. 2008). Vertical stratification of dust grains follows B. Dubrulle et al. (1995) with an α (N. I. Shakura & R. A. Sunyaev 1973) parameter of 10^{-2}.

Assumption 2: XUE 1 is constantly exposed to an interstellar FUV field characterized by $\chi = 10^5$. Hereafter, we adopt χ as the ratio of the local FUV field to that in the solar neighborhood from B. T. Draine (1978):

$$\chi \equiv \int_{91.2\,\rm nm}^{205\,\rm nm} \lambda u_\lambda d\lambda \Big/ \int_{91.2\,\rm nm}^{205\,\rm nm} \lambda u_{\lambda,\rm Draine} d\lambda, \quad (2)$$

where u_λ is the specific energy density. We assume here that the three-dimensional separation of XUE 1 from the neighboring O stars is not much larger than the projected separation ~0.5 pc (see Figure 1).

Next, we define the physical parameters and boundary conditions of a fiducial model for the XUE 1 disk. This fiducial model shares many similarities with the DIANA model for a standard T Tauri disk, introduced in P. Woitke et al. (2016; see their Table 3). However, our fiducial disk differs in the following key aspects: the strength of the external FUV irradiation, in response to our second working assumption; the grain composition, in response to our characterization of the continuum (Section 2.3.1); and the disk mass, which is an observationally motivated choice as explained below.

Disk mass. Since there is currently no direct or indirect tracer for the disk mass, we assume a fiducial dust mass of $M_{\rm d} = 10^{-6}\,M_\odot$. The fiducial gas mass is obtained by rescaling $M_{\rm d}$ by a canonical interstellar medium gas-to-dust ratio of 100 (e.g., J. P. Williams 2021), i.e., $M_{\rm g} = 10^{-4}\,M_\odot$. We note that our choice for the dust mass is within the range $0.1 - 1.0\,M_\oplus$, and is consistent with 60% of the stellar disks observed in Lupus and Chamaeleon (Ł. Tychoniec et al. 2018). Similar trends have been observed for disks in Orion, although limited by lower sensitivities (S. E. van Terwisga et al. 2022).

Disk size. We assume a fiducial tapering radius $R_{\rm tap} = 100$ au, following the DIANA standard T Tauri disk (P. Woitke et al. 2016). While this $R_{\rm tap}$ is consistent with the disk sizes observed in Ophiuchus and Taurus (A. Tripathi et al. 2017), it is not consistent with the substantially lower distribution of disk sizes observed in Orion (J. A. Eisner et al. 2018). In Sections 3.1.1 and 3.1.2, we present model-based evidence that rules out our initial assumption of $R_{\rm tap} = 100$ au, supporting a more compact configuration for the XUE 1 disk. Following E. Gullbring et al. (1998), the inner disk radius is assumed to be within the corotation radius, at $R_{\rm in} \equiv 5R_* = 0.07$ au, where R_* is the stellar radius.

Grain properties. We implement an MRN size distribution (J. S. Mathis et al. 1977) between a minimum and maximum grain sizes of 0.05 μm and 3 mm, respectively. The MRN distribution is also characterized by a slope p—this parameter plays an important role in determining the shape of the spectral energy distribution (SED) at long wavelengths in the mid-IR. The MNR distribution has a slope $p = 3.5$ as measured in the interstellar medium. However, detailed studies of spatially resolved disks seem to favor a range of values for the slope that go above and below 3.5 (e.g., E. Macías et al. 2021; G. Guidi et al. 2022; J. K. Doi & A. Kataoka 2023). In particular, values higher than $p = 3.5$ enhance the contribution of smaller grains to the total opacity and lead to a stronger 10 μm emission feature. For the fiducial model we adopt $p = 3.9$, which is similar to the value found with `ProDiMo` models for PDS 70 (B. Portilla-Revelo et al. 2022) and EX-Lupi (P. Woitke et al. 2024). The size distribution is discretized in 100 size bins. Grains are made of a mixture of carbonaceous (15% volume fraction) and silicate material (60%), with 25% of the volume of the aggregate assumed as vacuum. We analyze a small grid of models where only the continuum radiative transfer is solved and the SEDs are qualitatively compared to the MIRI continuum. This analysis suggests a crystallinity value of less than 5% by volume. Additionally, for the amorphous silicates found in Section 2.3.1, the abundance is suggested to be in a 10:10:1 ratio by volume. Table 2 lists the volume fractions of silicates distributed among the elemental species retrieved in Section 2.3.1. We assume that the composition inferred from the mid-IR emission applies everywhere in the disk. Although this assumption seems valid given the scarcity of data, we note that certain properties might vary across the disk. For example, the value of the crystallinity could be spatially dependent if localized regions of efficient grain growth existed in the disk (e.g., R. van Boekel et al. 2005).

Disk geometry. The fiducial model is a flared disk in radiative equilibrium. The gas scale height is parameterized as $H(r) = H_0(r/r_0)^\beta$. Values for the scale height at the reference distance (H_0 and r_0), as well as for the flaring exponent (β), are listed in Table 2. Values for the reference scale height and the flaring exponent are slightly fine-tuned to enhance the overall quality of the fit. Nevertheless, the value for these parameters listed in Table 2 are still within the ranges that explain the observed SEDs from other disks studied by the DIANA project (P. Woitke et al. 2019; T. Kaeufer et al. 2023). Notably, a larger value for the reference scale height is theoretically expected for an irradiated disk since in hydrostatic equilibrium $H \equiv c_{\rm s}/\Omega \sim \sqrt{T_{\rm gas}}$, where $c_{\rm s}$ is the sound speed and Ω is the Keplerian frequency. Finally, the inclination of the disk with respect to the plane of the sky is set to 60° following M. C. Ramírez-Tannus et al. (2023).

Interstellar UV radiation field. The UV component of the background interstellar radiation field ($I_\nu^{\rm ISM,UV}$) is assumed isotropic. It is modeled as a diluted blackbody at a temperature

Table 2
Parameters of the Best Representative Model for the XUE 1 Disk

Parameter	Value
Mass	$1.2\ M_\odot$
Bolometric luminosity ($L_{\rm bol}$)	$3.9\ L_\odot$
Effective temperature	4729 K
$L_{\rm FUV}/L_{\rm bol}$[a]	0.04
X-ray luminosity ($L_{\rm X}$)	2.5×10^{30} erg s^{-1}
X-ray emission temperature	3×10^7 K
Mass-accretion rate[b]	$1.76 \times 10^{-9}\ M_\odot$ yr^{-1}
Relative external FUV field (χ)	10^5
Minimum grain size	0.05 μm
Maximum grain size	3000 μm
Grain size power index	3.9
Porosity	25%
Amorph. carbon (by volume)	15%
Amorph. pyroxene ($Mg_{0.7}Fe_{0.3}SiO_3$)	26.2%
Amorph. olivine ($MgFeSiO_4$)	26.2%
Amorph. silica (SiO_2)	2.6%
Forsterite (Mg_2SiO_4)	2.5%
Enstatite ($Mg_{0.96}Fe_{0.04}SiO_3$)	2.5%
Turbulent settling parameter (α)	10^{-2}
Gas-phase carbon-to-oxygen ratio	0.457
Disk gas mass	$6.1 \times 10^{-5}\ M_\odot$
Disk dust mass	$0.3\ M_\oplus$
Inner radius	0.07 au
Tapering radius ($R_{\rm tap}$)	10 au
Inclination	60°
Flaring exponent (β)	1.30
Reference radial distance (r_0)	10 au
Scale height at r_0 (H_0)	1 au

Notes.
[a] We treat the stellar FUV luminosity as a free parameter. A $L_{\rm FUV}$ value that is due to accretion only cannot explain the strength of the CO emission. This suggests that chromospheric activity plays a major role in setting the FUV luminosity of XUE 1.
[b] Average value observed in Taurus by C.-L. Lin et al. (2023).

20,000 K (P. Woitke et al. 2016),

$$I_\nu^{\rm ISM,UV} = \chi \cdot 1.71 W_{\rm dil} \cdot B_\nu(20,\,000\ {\rm K}), \quad (3)$$

with $W_{\rm dil} = 9.85357 \times 10^{-17}$, a dilution factor such that $\chi = 1$ (see Equation (2)) corresponds to the UV radiation field in the solar neighborhood. The DIANA standard model has $\chi = 1$ and our fiducial model has $\chi = 10^5$.

ProDiMo first solves the continuum radiative transfer and then iterates over the gas heating–cooling balance and the chemistry. Iterations are needed since the gas temperature and molecular abundances depend on each other. ProDiMo computes the gas temperature by balancing several heating and cooling mechanisms; this step requires knowing the level populations of the gas species included in the model. Level populations are computed assuming either LTE or non-LTE conditions, depending on the availability of collisional data. The levels of C_2H_2, HCN, and CO_2 are all populated according to LTE. A non-LTE treatment is followed for H_2O (collision data are taken from the LAMDA database; see F. L. Schöier et al. 2005; F. F. S. van der Tak et al. 2020 and references therein); pure rotational OH lines (A. R. Offer et al. 1994; U. Rahmann et al. 1999; B. Tabone et al. 2021); and for CO, for which the custom molecular model by W. F. Thi et al. (2013) is used. Spectroscopic data are mostly taken from the HITRAN (I. E. Gordon et al. 2022) and LAMDA databases. An escape probability formalism determines the excitation and deexcitation rates. For the chemistry, we use the large chemical network from I. Kamp et al. (2017) with 236 species and 3046 chemical reactions. Creation and destruction processes and their respective rate coefficients are mostly taken from the UMIST database (D. McElroy et al. 2013). For a description of a few additional processes that are not in UMIST—such as freeze-out and desorption ice chemistry, and H_2 formation via dust catalysis—we refer the reader to P. Woitke et al. (2024) and references therein for details. Finally, ray-tracing and line-escape probability algorithms are used to generate synthetic SEDs and emission line spectra.

3. Results

3.1. Physical Structure of the XUE 1 Disk: Dust and Gas Distribution

3.1.1. Dust Distribution

The model for the fiducial disk performs poorly in explaining the observations. Notably, the response to an enhanced FUV irradiation is evident on the continuum: the synthetic SED displays very strong mid- and far-infrared emission that is not consistent with the observations (see left panel in Figure 3). To quantify this discrepancy, we use the spectral index

$$n_{13-25} \equiv \frac{\log(\lambda_{25}F_{25}) - \log(\lambda_{13}F_{13})}{\log(\lambda_{25}) - \log(\lambda_{13})}, \quad (4)$$

where F_λ is the specific flux and the wavelength λ is in microns. The spectral index predicted by the fiducial model is 1.80 times higher than the observed one $n_{13-25}^{\rm obs} = 5.53$. This behavior is a consequence of Kirchhoff's law—the mass absorption coefficient of the dust distribution implies a high efficiency of absorption of UV photons, which in turn implies an efficient re-emission at infrared wavelengths.

For a flared disk in radiative equilibrium, the emission in the $10 \lesssim \lambda \lesssim 100\ \mu$m range is dominated by an optically thin surface of dust (E. I. Chiang & P. Goldreich 1997). Thus, the flux scales with the disk's solid angle as seen from the observer. Accordingly, we reduce the disk's size by cutting the tapering radius down from 100 au to 10 au, while keeping the dust mass constant. This change renders the fiducial disk into a compact disk, for which the emitting area decreases and the density in the inner regions increases. The synthetic SED from the compact disk has a spectral index that is only 1.01 times the observed one. We note that our choice of $R_{\rm tap} = 10$ au comes from comparing only the observed to synthetic spectral indexes. A thorough study on the effect of the tapering radius on the synthetic line emission, as well as the impact of polycyclic aromatic hydrocarbons (PAHs), will be presented in S. Hernández et al. (2025, in preparation). We also disregard the tidal effects from the A2 component (the secondary member of the binary pair). The compactness of the system and the relatively low mass of the secondary (Section 2.1) make it unlikely that tidal effects could truncate the disk below 10 au (O. Panić et al. 2021). Similarly, we neglect any heating contribution due to the radiation field set by the companion.

The continuum emission at near and short mid-IR wavelengths is sensitive both to the geometry and to the density

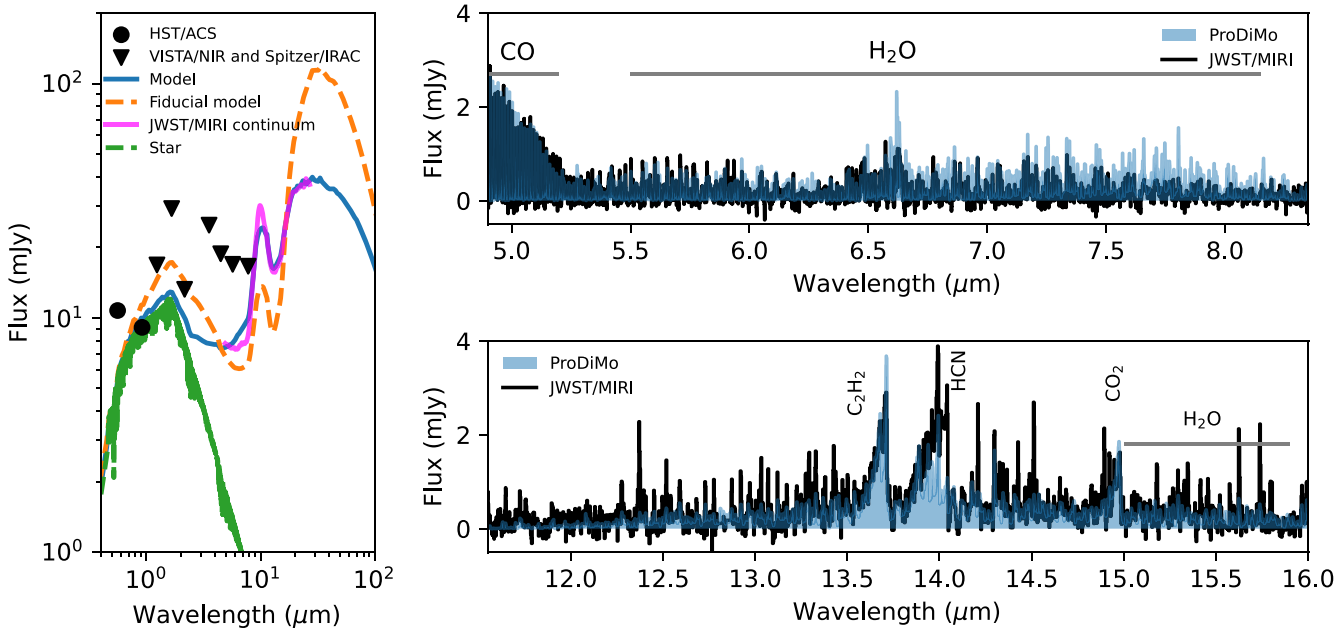

Figure 3. Synthetic predictions from the XUE 1 model against the observations. Left: photometry toward XUE 1; dots indicate the HST/ACS photometry and downward arrows indicate upper limits from VISTA and Spitzer. The magenta line is the JWST/MIRI continuum. The green is the stellar spectrum, and the blue and orange lines indicate the spectral energy distributions of the best-fit and fiducial disk models, respectively. Right: continuum-subtracted spectra for MIRI channels 1 (top) and 3 (bottom); the black curves are the MIRI data and the areas filled in blue are the `ProDiMo` spectra. Synthetic spectra are convolved using a Gaussian kernel with $R = 3500$ for channel 1 and $R = 2500$ for channel 3.

distribution near the disk's inner rim (C. P. Dullemond & J. D. Monnier 2010). These two properties determine the radial optical depth in the inner disk. Equation (1) implies a step function-like transition of the density at the inner radius. Since this is clearly unrealistic, we further modify the initial dust density profile to allow for a gradual build up of solid material from the inner radius outwards. This is modeled as a depletion of the initial profile by a Gaussian function centered at $r = 0.6$ au with a standard deviation of 0.15 au.[21] The center of the Gaussian and its standard deviation come from a small grid of models aimed at explaining the observed NIR photometry and the MIRI continuum around the 10 μm feature. This approach is similar in nature to the method introduced in P. Woitke et al. (2024) to simulate the gradual build up of dust near the inner rim. However, our approach can treat the dust and gas density distributions independently from each other. Figure 4 shows the dust surface density profiles for both the fiducial and best-fit models. We highlight that the dust surface density at 0.13 au—where the equilibrium temperature of a grain reaches the silicate sublimation threshold of 1500 K—is four orders of magnitude lower compared to the unperturbed profile of the fiducial model. Qualitatively, this is in accordance with what is expected in the presence of dust sublimation driven by stellar radiation.

The synthetic SED from the best-fit model is compared to the observation in the left panel of Figure 3. Integrating the final surface density profile over the radial and azimuthal coordinates, we find a dust mass of 0.3 $M_\oplus$. Thus, the dust mass of the best representative model is only 10% lower than the initial value, due to the enforced dust depletion near the inner rim.

[21] The choice of a Gaussian function is arbitrary. However, this is a simple way to simulate smooth changes in density that are also axisymmetric. This approach has also been applied to describe the dust distribution near gaps and cavities in disks (e.g., M. Keppler et al. 2018).

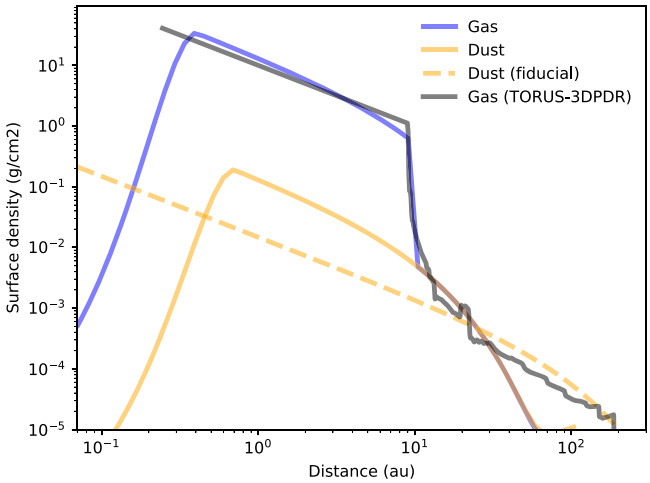

Figure 4. Surface density profiles of dust and gas as a function of semimajor axis. Solid curves indicate the solution from the best representative model for XUE 1. The dashed line indicates the dust surface density of the fiducial disk. Black line is the steady-state solution of the radiation-hydrodynamical model discussed in Section 4.3.

3.1.2. Gas Distribution

We generate a continuum-subtracted spectrum starting from the disk model that already explains the continuum (Section 3.1.1). We first focus on the wavelength range covered by MIRI channel 1. As observed in nearby disks around T Tauri stars, this spectral window shows prominent emission from H_2O and CO (D. Gasman et al. 2023; Á. Kóspál et al. 2023; G. Perotti et al. 2023; T. Henning et al. 2024). This is also the case for the XUE 1 disk (M. C. Ramírez-Tannus et al. 2023).

The synthetic spectrum showed an emission feature around 5.4 μm that contrasts with the data: the P-, Q-, and R-branches of nitrogen monoxide (NO) rovibrational emission (Figure 5,

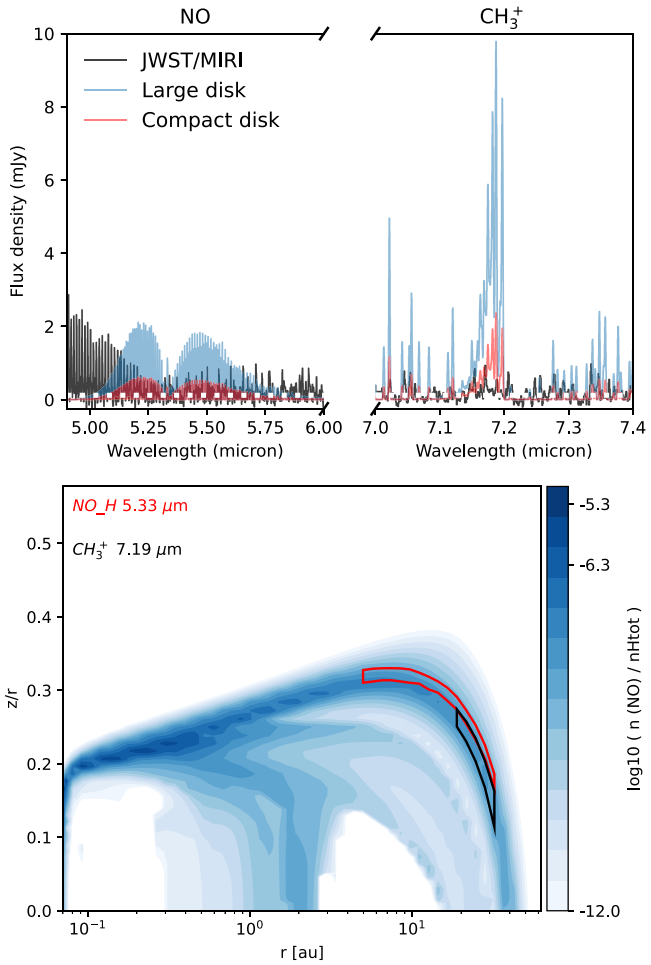

Figure 5. Synthetic predictions for NO and CH_3^+. Top: continuum-subtracted spectra—blue and red lines are from the fiducial and compact disks, respectively. The black line is the MIRI observation and the white dots indicate the noise level. The observed features below 5.2 μm correspond to the P-branch of the CO rovibrational emission. Bottom: emitting areas of the NO (red box) and CH_3^+ (black box) emission retrieved from the compact disk. Color map shows the gas-phase abundance of NO relative to the total hydrogen nuclei.

top). For the compact disk, the strength of this feature is more than twice the noise level; for the fiducial disk, the strength is almost 10 times the noise level. Further inspection of the models revealed that this emission originates in the outer disk —beyond 15 au for the compact disk (Figure 5, bottom), and beyond 30 au for the fiducial disk.

NO is a diatomic molecule whose formation and destruction pathways, for large r and z values, proceed, respectively, via (K. R. Schwarz & E. A. Bergin 2014):

$$\begin{aligned} \mathrm{N} + \mathrm{OH} &\rightarrow \mathrm{NO} + \mathrm{H}, \\ \mathrm{N} + \mathrm{NO} &\rightarrow \mathrm{N2} + \mathrm{O}, \end{aligned} \tag{5}$$

and thus, a high abundance of NO should be accompanied with a high abundance of OH. In dense environments, formation of OH via dissociative recombination of $H3O^+$ is favored by a large abundance of free electrons.[22] In an irradiated disk, FUV photoionization of abundant species such as carbon and sulfur, increases the number of free electrons in the disk. Likewise, gas-phase oxygen chemistry driven by warm H_2 leads to OH formation via the reaction $H_2 + O \rightarrow OH + H$, a process recently observed in the environment of an irradiated disk in Orion (M. Zannese et al. 2024). These arguments naturally explain the high abundance of NO both in the fiducial and compact disks, which are both strongly irradiated.

While a lower abundance of free electrons (i.e., a weaker external FUV field) can reduce that of NO in the outer disk, a lower gas surface density beyond 10 au can also have the same effect. We explore the latter option and defer the former for the discussion. We deplete the gas mass beyond 10 au by factors of 10 and 100 with respect to the nominal values in the fiducial model—the latter depletion factor implies a gas-to-dust ratio of 1.0 in the outer disk. This gas-depleted and compact disk shows no NO emission above the noise level, in accordance to the observation.

One caveat is that our model is limited by the lack of collisional data for NO, and therefore we assume LTE for its level populations. However, since the NO emission comes from the outer disk (Figure 5), LTE might not accurately reflect the excitation conditions in this low-density area. We estimate a volume-weighted average abundance of total hydrogen nuclei within the NO emitting region of $\langle n(\mathrm{H_{tot}})\rangle = 3.0 \times 10^7\,\mathrm{cm^{-3}}$. A non-LTE approach could result in lower upper state population densities, as seen with other molecules like CO (W. F. Thi et al. 2013). Thus, non-LTE effects might reduce the need to remove gas from the outer disk. A detailed study of NO's spectral signature requires rovibrational collisional data, which is currently unavailable in the literature. Determining these collisional coefficients is well beyond the scope of this work.

Motivated by the recent detection of CH_3^+ in the wind of an irradiated disk in Orion (O. Berné et al. 2023), we generate a synthetic spectra for this molecule in MIRI/channel 1.[23] Similar to NO, our model predicts a very strong emission feature around $\sim$7.2 μm, which contrasts sharply with the observation. The bottom panel in Figure 5 shows that this emission also originates from the outer disk. Since we do not detect CH_3^+ in the XUE 1 disk, we interpret this result as further evidence for the need of gas depletion in the outskirts of the disk.

Finally, starting now from the compact and outer gas-depleted disk, we generate a synthetic spectrum that covers MIRI channel 3, where strong emission from C_2H_2, HCN, and CO_2 is observed in XUE 1 (M. C. Ramírez-Tannus et al. 2023). The synthetic spectra already agree with the observation within a factor of 2 for each of those molecules.

The largest discrepancy occurs in channel 1, where `ProDiMo` predicts water lines that are up to a factor of 4 stronger than the observation. The model indicates that the emitting region of those lines is restricted to the inner 1 au (see Section 4.1 for a discussion on line-emitting regions). We take the o-H_2O $\lambda \approx 6.62\,\mu$m line as a proxy: this line has an emitting region that extends vertically from $z/r = 0.16$ down to $z/r = 0.045$, and radially from $r = 0.07$ au out to $r = 0.4$ au. In

[22] For the fiducial disk externally irradiated with $\chi = 10^5$, the electron abundance averaged over the emitting region of NO is $\mathcal{O}(10^3\,\mathrm{cm^{-3}})$. For the nonirradiated fiducial disk ($\chi = 1$), the averaged electron abundance is only $\mathcal{O}(10^2\,\mathrm{cm^{-3}})$.

[23] The reader is cautioned that all results related to CH_3^+ were obtained using a beta version of `ProDiMo`, rather than the current stable version (v3.0.0) used in the rest of the paper. While we acknowledge the potential limitations this may introduce for reproducibility, we believe the results are robust enough to be included in this manuscript.

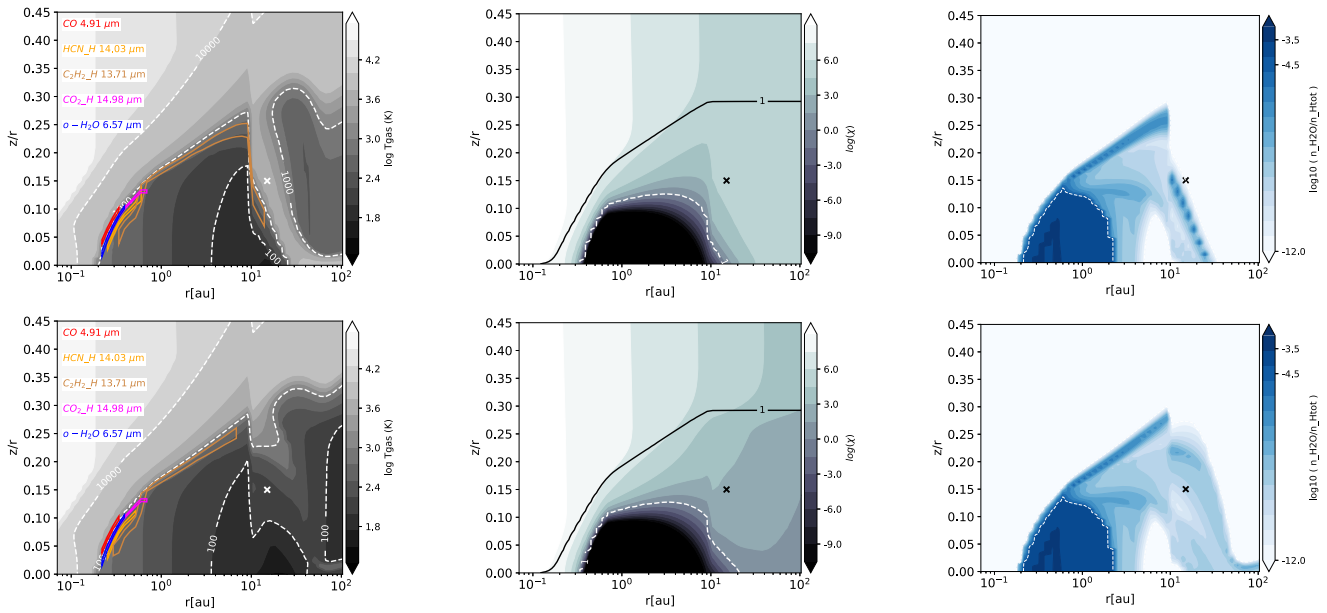

Figure 6. Two-dimensional maps in disk aspect ratio vs. radial distance space for selected disk properties. The top row contains the solution from the best representative model for the XUE 1 disk ($\chi = 10^5$); the bottom row shows the solution from a nonirradiated disk ($\chi = 10^0$) with the same gas and dust composition and structure. Left panels: the grayscale image shows disk gas temperature with isothermal contours in white dashed lines. The color boxes depict the 15%−85% emitting areas of the lines that are indicated in the upper-left corner of the figure. Middle panels: strength of the UV radiation field in units of the Draine field—dashed contour indicates the region in the disk that is exposed to an FUV strength equal to the value in the solar neighborhood. Solid contour indicates the region where the radial optical depth is one. Right panels: abundance of gas-phase water relative to the total number of hydrogen nuclei—dashed line encloses 90% of the total abundance. The quantitative analyses presented in Sections 3.1.2 and 3.2 are done at the grid point indicated by the cross.

order to reduce the o-H_2O $\lambda \approx 6.62\,\mu$m line strength in the model, we modify the inner disk gas distribution using a Gaussian depletion function centered at $r = 0.4$ au. Exploration of a coarse grid of models suggests a value for the standard deviation of 0.07 au. We determine this value for the standard deviation by visually comparing the synthetic and observed line fluxes in channels 1 and 3. A stronger depletion would further improve the fit to the water features (by making them weaker), but it would underfit the CO flux in the P-branch. The final gas density profile is shown in Figure 4.

Table 2 summarizes the parameters of the best-fit model. The continuum-subtracted synthetic spectra are compared to the observations in the right panel of Figure 3. Integrating the gas surface density yields a total gas mass of $\sim 6 \times 10^{-5}\,M_\odot$ for the XUE 1 disk.

3.2. Physical Structure of the XUE 1 Disk: Gas Temperature and Molecular Abundance

The two-dimensional gas temperature from the best representative model is shown in the top-left panel in Figure 6. The vicinity of the inner radius ($r \lesssim 0.1$ au) is characterized by gas temperatures of $\sim 10^4$ K; similar values are found in the upper disk layers ($z/r \gtrsim 0.5$) at all radii. Close to the midplane, the temperature varies with distance: toward the optically thin dust rim, the temperature drops to 1000 K; for $0.2 \lesssim r \lesssim 3$ au—where most of the MIRI emission originates—temperature ranges from 1000 K down to 100 K; and for $3 \lesssim r \lesssim 10$ au, gas temperature remains below 100 K. Interestingly, for $r > 10$ au, the temperature increases again in response to the external irradiation.

The gas temperature at each grid cell in the computational domain results from balancing out many heating and cooling processes. The final model includes a total of 103 heating processes and 95 cooling processes. Notably, FUV photons play an important role in relevant heating mechanisms, such as photoelectric and photochemical heating (e.g., I. Kamp et al. 2024). To quantify the effect of the external irradiation on the temperature, we simulate the XUE 1 disk again, but this time assuming it is not strongly irradiated with $\chi = 1.0$. The resulting gas temperature distribution is in the bottom-left panel of Figure 6.

Let us analyze an arbitrary point in the disk, the one with coordinates $\mathcal{P} = (15\text{ au}, 0.15)$, which is indicated by the crosses in Figure 6. For the irradiated disk, the magnitude of the total heating function at that point is $\Gamma_{\rm tot} = 7.1 \times 10^{-15}\,{\rm erg\,cm^{-3}\,s^{-1}}$. For the nonirradiated disk, we find $\Gamma_{\rm tot} = 1.8 \times 10^{-15}\,{\rm erg\,cm^{-3}\,s^{-1}}$—this is 4 times lower than for the irradiated disk. Furthermore, the leading heating mechanism when $\chi = 10^5$ is dissociative heating of H_2; on the contrary, when $\chi = 1.0$, the leading heating mechanism is heating by dust thermal accommodation. Overall, these differences imply a gas temperature at $\mathcal{P}$ of $T_{\rm g} = 3791$ K (irradiated) and $T_{\rm g} = 158$ K (nonirradiated). Similarly, the dust temperatures are $T_{\rm d} = 99$ K (irradiated) and $T_{\rm d} = 72$ K (nonirradiated).

Interestingly, points to the right of $\mathcal{P}$ that are at the same height display higher gas temperatures. Quantitatively, this is explained because the total heating function for those points at larger radii is $\sim$100 times lower than at $\mathcal{P}$. Also, different heating and cooling mechanisms dominate at each region: Dissociative heating of H_2 and Lyα cooling dominate at $\mathcal{P}$, whereas PAH heating and O I line cooling dominate at larger radii. This demonstrates the complex interplay between the heating–cooling balance and the chemistry involved in a self-consistent solution to the equilibrium gas temperature.

The solution of the continuum radiative transfer determines the strength of the FUV field at each location in the disk. The

Table 3
Physical Properties within the Emitting Regions of Mid-IR Lines for the XUE 1 Disk

Molecule	Vibrational Quantum Numbers[a]	No. Lines	$\langle T_{\rm gas}\rangle$ (K)	$\log(\langle N\rangle)$ ($\rm cm^{-2}$)	$\langle R_{\rm eff}\rangle$[b] (au)	$T_{\rm ex}$ (K)	$\log(N)$ ($\rm cm^{-2}$)	R (au)
			This Study			M. C. Ramírez-Tannus et al. (2023)		
H_2O [7 μm]	0 1 0 → 0 0 0	769	634 ± 75	20.0 ± 0.6	0.33	975	18.3	0.13
H_2O [15 μm]	0 0 0 → 0 0 0	646	608 ± 88	20.0 ± 0.7	0.38	550	19.8	0.46
HCN	0 1 1 0 → 0 0 0 0	211	540 ± 87	19.0 ± 1.3	0.37	575	17.3	0.57
C_2H_2	000 0 1 0 1 u → 000 0 0 0+ g	726	527 ± 89	18.3 ± 2.2	2.7	475	18.3	0.23
CO_2	0 1 1 01 → 0 0 0 01	126	574 ± 147	17.3 ± 0.4	0.55	450	14.3	5.30
CO	1 → 0	98	1343 ± 278	19.8 ± 0.8	0.27	2300	17.5	0.44

Notes. The third column lists, for each species, the number of lines used to compute the averaged properties.
[a] The quantum numbers are for the vibrational band that contains the strongest transition within a given wavelength range. For HCN, CO_2, and C_2H_2, the listed bands include the peaks of the Q-branches at $\lambda \sim 14.04$, 14.98, and 13.71 μm, respectively. For CO, the band includes the strongest transition of the P-branch observable with MIRI in channel 1. For H_2O, the bands contain the strongest transition in the intervals 5−8 μm (rovibrational) and 15−16 μm (pure rotational), respectively. Quantum number notation follows HITRAN convention (I. E. Gordon et al. 2022).
[b] Let $\langle R_{15}\rangle$ and $\langle R_{85}\rangle$ be the flux-weighted average distances where the cumulative flux reaches 15% and 85%, respectively. We define $\langle R_{\rm eff}\rangle$ as the radius of a circle whose area equals that of an annulus with inner and outer radii $\langle R_{15}\rangle$and $\langle R_{85}\rangle$; this is, $\langle R_{\rm eff}\rangle^2 \equiv \langle R_{85}\rangle^2 - \langle R_{15}\rangle^2$.

FUV radiation field (in units of the Draine field) are shown in the middle panels in Figure 6. At $\mathcal{P}$, we find $\log(\chi/\chi_{\rm Draine}) = 4.7$ for the irradiated disk; for the nonirradiated disk, we find $\log(\chi/\chi_{\rm Draine}) = 2.9$ at the same location. We repeat this calculation at a different grid point with coordinates $r = 0.3$ au and $z/r = 0.1$. This is a characteristic location in the disk from where several of the features observed by MIRI are emitted. At this location, the strength of the FUV field in the irradiated disk is indistinguishable from that in the nonirradiated disk. Clearly, this implies that the FUV field interior to 1 au is entirely set by the central star.

Given the dependence of the molecular abundances on the gas temperature, it is expected that the external irradiation will affect such abundances in the outer disk. We focus on the gas-phase abundance of water in the XUE 1 disk. Right panels in Figure 6 display the distribution of water in the irradiated (top) and nonirradiated (bottom) cases. The fractional abundances at $\mathcal{P}$ are $n_{\rm H_2O}/n_{\rm Htot} = 7.1 \times 10^{-13}$ and 6.8×10^{-10}, for the irradiated and nonirradiated cases, respectively ($n_{\rm Htot}$ is the total hydrogen number density). At this grid point, the total destruction rate of water (which is equal to the total formation rate because steady state is assumed) is $k^{\rm tot}_{\rm H_2O} = 4.5 \times 10^{-10}\,\rm cm^{-3}\,s^{-1}$ for the irradiated disk, and $k^{\rm tot}_{\rm H_2O} = 2.2 \times 10^{-9}\,\rm cm^{-3}\,s^{-1}$ for the nonirradiated disk. The model also suggests that the leading destruction mechanism of water in the first case is the neutral–neutral two body reaction: $\rm H + H_2O \rightarrow OH + H_2$. In contrast, for the second case, the leading destruction mechanism is the photoreaction $\rm H_2O + \gamma_{UV} \rightarrow OH + H$.

Although the water abundance at $\mathcal{P}$ is lower in the irradiated disk, the right panel in Figure 6 also suggests an enhanced abundance for lower values of z/r, compared to the nonirradiated disk. To quantify this effect, we retrieve from the model the water surface density profile and perform the surface integral to find the mass of water that is contained in the outer disk, i.e., we integrate radially from 10 to 100 au. For the irradiated disk the gas-phase water reservoir is $2.2 \times 10^{-13}\,M_\odot$; for the nonirradiated disk, the gas-phase water reservoir is $4.4 \times 10^{-15}\,M_\odot$. Therefore, our model predicts an enhancement by a factor of 100 in the gas-phase water reservoir in the outskirts relative to a nonirradiated disk. However, the observability of those tracers is expected to be compromised by their low abundance in absolute numbers, due to the depletion effect of the photoevaporating winds.

4. Discussion

4.1. Emitting Regions of Mid-infrared Lines

M. C. Ramírez-Tannus et al. (2023) report key physical properties for the XUE 1 disk such as molecular column densities, excitation temperatures, and characteristic sizes of emitting regions, for those lines detected with MIRI. Those properties were derived via slab-modeling the spectra in channels 1 and 3. We perform a similar characterization based on our best representative thermochemical model (Section 3). Note, however, that comparing the results from both approaches must be done with care. While in slab models the retrieval of column densities, temperatures, and emitting areas is driven by the data, in thermochemical models those quantities are inferred from the physics that explains the data. Thus, we attempt only a ballpark comparison.

We first fetch information about the spatial extent from which a given molecular species emits at a specific wavelength. For a molecule emitting at a certain wavelength, we define its emitting area as the spatial region that encloses 15% to 85% of the line flux, in both the radial and vertical directions (top-left panel in Figure 6 displays emitting areas of individual lines for a few molecules). Furthermore, the slab models were constrained not by a single line, but by a series of lines spanning a range of wavelengths (see Table 3 in M. C. Ramírez-Tannus et al. 2023). Consequently, we compute the mean values and standard deviations of each of the aforementioned quantities by averaging the flux-weighted quantity over the spatial and spectral coordinates (i.e., we use Equation (76) in P. Woitke et al. 2024).

Results are in Table 3 where we also include the values from M. C. Ramírez-Tannus et al. (2023). Physical properties derived from the thermochemical model are in broad agreement with the slab models. Some expected trends—such as larger emitting areas for water lines in channel 3 than in channel 1, as well as a gradient in their excitation temperatures (A. Banzatti et al. 2023)—are seen in both approaches. On the other hand, the largest discrepancy occurs with CO_2. The slab model retrieves a large emitting area that compensates for a distinctly

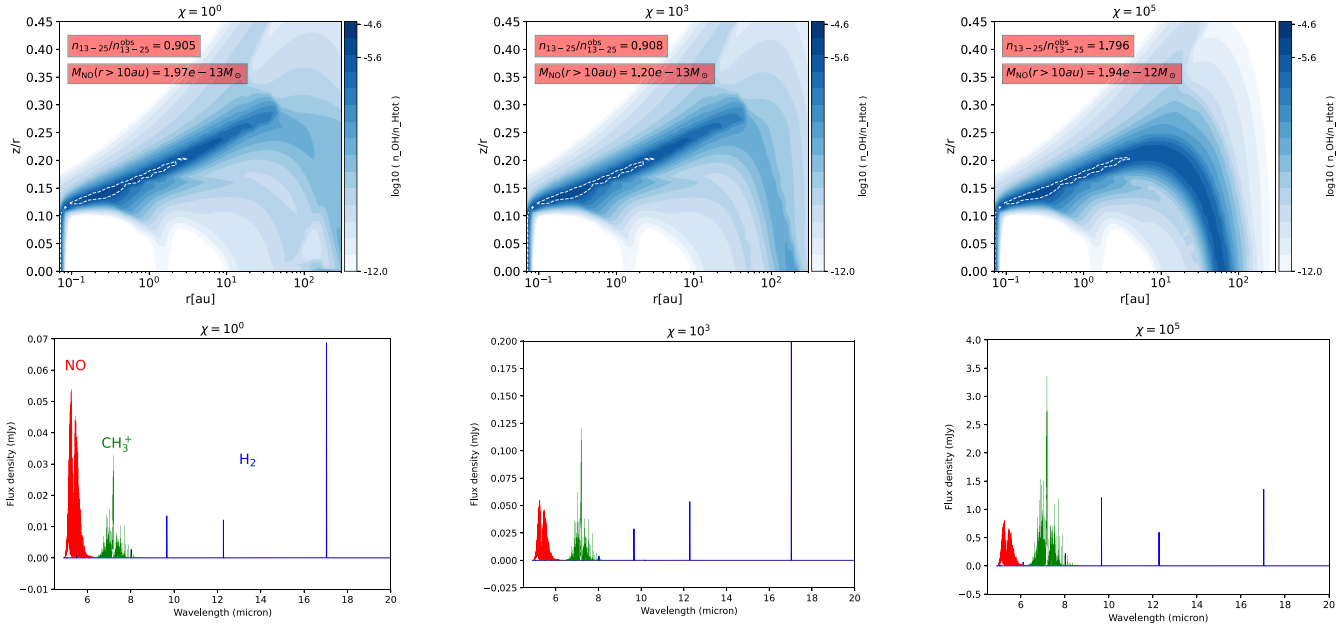

Figure 7. Effect of external irradiation on the physical structure and line emission of the fiducial disk. Top: two-dimensional distribution of gas-phase OH for different realizations of the fiducial disk. Each realization corresponds to a different value of χ. Dashed lines enclose 90% of the total abundance of OH. The insets display for each model the ratio of the synthetic spectral index to the observed one and the corresponding mass of NO contained beyond 10 au. Bottom: synthetic spectra for NO, H_2, and CH_3^+. Note the difference on the vertical scale.

low column density that falls in the optically thin regime, causing $\log(N)$ and R to become degenerate.

The emitting areas depicted in Figure 6 suggest that most of the emission observed with MIRI primarily originates in the inner 1 au of a compact and outer gas-depleted disk. In that inner region the effects of the external irradiation are negligible (Section 3.2). This explains why the MIRI spectrum of XUE 1 looks so similar to those of nearby, nonirradiated disks.

4.2. Parameter Degeneracy: Is the XUE 1 Disk Truncated by Photoevaporation or Shielded Against FUV Photons?

While the parameters listed in Table 2 are derived from physical considerations, those are not the only parameters capable of explaining the observations. This is because our model—just like any other thermochemical model—suffers from multiple degeneracies among its many different parameters (e.g., P. Woitke 2015; P. Cazzoletti et al. 2018).

There is one degeneracy worth discussing in the context of this work relating the disk's size (parameterized in our model by $R_{\rm tap}$) and the strength of the external FUV field (parameterized by χ). This degeneracy implies that the same set of observables could be reproduced if we modeled XUE 1 as a larger disk, but subjected to a weaker external FUV field. In fact, numerical simulations have showed that disks can be shielded from FUV radiation by the residual dust and gas material from the star formation process (L. Qiao et al. 2022; M. J. C. Wilhelm et al. 2023).

We generate six realizations of the fiducial model (Section 2.3.2) for different values of χ, from 10^5 down to 10^0. Figure 7 shows the effect of varying χ on both $n_{13-25}/n_{13-25}^{\rm obs}$ and the abundance of OH (the precursor of NO, see Equation (5)), for $\chi = 10^0$, 10^3, and 10^5. The spectral index reacts to the external irradiation only when $\chi \geqslant 10^3$. This means that if our second assumption—concerning XUE 1 being constantly exposed to $\chi = 10^5$—did not accurately capture the actual irradiation environment of XUE 1, and instead overestimated it by at least a factor of 100, then the larger fiducial disk could be just as capable of reproducing the observed spectral index as the smaller, strongly irradiated disk.

Additionally, Figure 7 quantifies how the gas-phase reservoir of NO beyond 10 au changes with the strength of the external UV field. For $\chi \leqslant 10^3$, the mass of NO in the outer disk fluctuates closely around a mean value of $1.6 \times 10^{-13} M_\odot$. However, for $\chi > 10^3$, the NO mass increases substantially, reaching values up to 10 times higher than the mean value at $\chi \leqslant 10^3$. Again, this means that if our second assumption did not hold, removing gas from the outer disk would not be required to explain the nondetection of NO; the solution to the chemistry by itself would lead to a lower abundance of NO in the outskirts of the disk.

To break this degeneracy, we need to gather more information on two critical aspects. First, a deeper characterization of the OB star population in the Pismis 24 subregion is necessary. This includes creating a three-dimensional map for the locations of the ionizing sources relative to XUE 1. This is, however, challenging due to the limitations of current observational facilities. Second, we need better constraints on the local interstellar medium around XUE 1, which involves identifying and characterizing any potential sources of obscuration between the ionizing sources and XUE 1.

Clearly, this degeneracy could also be resolved in an ensemble sense; this is, by observing and forward modeling a population of irradiated disks, as we did here for XUE 1. Given the large distances to high-mass SFRs, JWST capabilities are key to achieve this goal.

In Figure 7, we also examine the effect of irradiation strength on the synthetic spectra of NO, H_2, and CH_3^+. For NO, we observe a trend similar to that seen for the continuum slope and OH abundance: line fluxes remain comparable for $\chi \leqslant 10^3$, but increase by more than an order of magnitude when $\chi = 10^5$. Both CH_3^+ and H_2 exhibit greater sensitivity to external irradiation, with a 2 order of magnitude increase in flux from

$\chi = 1$ to 10^5. Since neither CH_3^+ nor H_2 are robustly identified in the XUE 1 spectrum, these findings suggest that a larger disk could potentially explain the observations, but only if $\chi < 10^3$.

4.3. Comparison with Radiation-hydrodynamical Models of Photoevaporated Disks

Our best representative model suggests a compact and low-mass disk around XUE 1. Truncation of disks is expected in high-FUV environments (e.g., C. J. Clarke 2007; G. A. L. Coleman & T. J. Haworth 2022); however, our calculations impose a depleted hydrostatic profile beyond 10 au that might not necessarily reflect the structure of a photoevaporative wind as a hydrodynamic flow. We check this by comparing with bespoke radiation hydrodynamic simulations of the wind for disk parameters suggested by our best representative model, calculated using the `TORUS-3DPDR` code (T. G. Bisbas et al. 2015, 2012; T. Harries et al. 2019). `TORUS-3DPDR` performs photodissociation region (PDR) and hydrodynamic calculations iteratively to solve for the steady-state wind structure. These models are extensively used in the FUV Radiation Induced Evaporation of Disks (FRIED) grids (see T. J. Haworth et al. 2018, 2023, for further details). These calculations are FUV-only and so only apply to the wind interior to the ionization front; however, that is sufficient here given our main focus is on the surface density profile close to the disk outer edge. We retrospectively calculated how deep into the FUV-only model ionizing radiation would penetrate by solving ionization equilibrium on a cell-by-cell basis assuming hydrogen only gas. Geometrically diluting the ionizing radiation from the UV sources in the cluster yields an ionizing flux at XUE 1 of 1.59×10^{13} photons $cm^{-2}\,s^{-1}$, in which case the ionization front only makes it 0.1 au into the grid. That estimate also does not account for material beyond the grid edge, nor the fact that the incident ionizing flux may be further attenuated by the true separation from the UV sources being larger than the projected, as well as dust absorption.

Our model for the XUE 1 disk (Section 3) serves as boundary condition for the `TORUS-3DPDR` simulation. Accordingly, we adopt a value of 10 au as the radius of the `TORUS-3DPDR` disk; that is, the $R_{\rm tap}$ parameter of the `ProDiMo` model is taken as the inner boundary for the photoevaporative flow in the `TORUS-3DPDR` model.

The rationale behind our choice of $R_{\rm tap}$ as the flow's inner boundary is twofold. First, our choice can be heuristically motivated by the necessity to remove gas beyond 10 au to explain the nondetection of NO (Section 3.1.2). Second, `ProDiMo` predicts values above 1000 K for the gas temperature for $r > 10$ au (see Figure 6)—these temperature values are comparable to the threshold $T_{\rm g} \lesssim 3000$ K that `TORUS-3DPDR` assumes when labeling a given cell as a PDR (T. G. Bisbas et al. 2015).

The gas density structure for $r < 10$ au is kept fixed to the value that explains the JWST/MIRI data. The initial surface density profile is modeled as $\Sigma(r,\, t = 0) = \Sigma_{1\ {\rm au}}(r/{\rm au})^{-1}$, with $\Sigma_{1\rm au} = 10\,{\rm g\,cm^{-2}}$, which is also informed by the `ProDiMo` model (see Figure 4). For the flow, we adopt a gas-to-dust ratio of 10^4—this means that we treat the dust population in the disk as an evolved one. This treatment aligns with our adoption of a dust size distribution for the disk, where grains as big as 3 mm are allowed to be present. In view of such size distribution ruling the disk opacity, and considering that grains larger than 0.1 μm are not expected to be entrained in the flow (S. Facchini et al. 2016), it is logical to assume that most of the dust mass will remain in the disk, which implies a dust-depleted flow. We use a mean grain cross section of $\sigma_{\rm grain} = 5.5 \times 10^{-23}\,{\rm cm^{-2}}$ to set the opacity in the flow.

We let the simulation run until the flow structure achieves steady state. The resulting gas surface density is depicted in Figure 4 (black curve). The steady-state solution for $r > 10$ au is in good agreement with the parameterized density structure from `ProDiMo`. This suggests that, for this particular combination of star, disk, and FUV field parameters, the inner wind behaves more like a hydrostatic atmosphere attached to the disk, which explains why this approximation is effective.

The `TORUS-3DPDR` calculation yields a mass-loss rate $\dot{M}_{\rm wind} = 5 \times 10^{-10}\,M_\odot\,{\rm yr^{-1}}$. This value combined with the inferred disk mass (Section 3.1.2) implies a depletion timescale $\tau_{\rm depletion} \equiv M_{\rm disk}/\dot{M}_{\rm wind} \approx 0.12$ Myr, which is similar to the values inferred from proplyds in the Orion Nebula Cluster (e.g., W. J. Henney & C. R. O'Dell 1999).

Accounting for both non-LTE effects in the thermochemical solution of NO (Section 3.1.2) and potential shielding mechanisms against FUV photons (Section 4.2) may increase our disk mass estimate. Consequently, the wind depletion timescale derived in this section should be interpreted as a lower limit.

5. Conclusions

In this work, we analyze JWST/MIRI spectroscopic and archival photometric data of the externally irradiated protoplanetary disk around the T Tauri star XUE 1. The XUE 1 disk is part of NGC 6357, a high-mass SFR with a UV radiation environment that surpasses those in nearby SFRs due to its higher density of O-type stars. Our analysis is conducted by building a thermochemical model for the disk that is capable of self-consistently explaining the available set of observations: V and Z bands HST/ACS photometry; J, H, K_s VISTA/NIR and [3.6 μm], [4.5 μm], [5.8 μm], and [8.0 μm] Spitzer/IRAC upper flux limits; JWST/MIRI continuum; and the JWST/MIRI molecular emission across channels 1 and 3. We infer from this model one set of suitable parameters that characterize the disk's physical structure. Our main conclusions are as follows:

1. We confirm the presence of amorphous (SiO_2, $Mg_{0.7}Fe_{0.3}SiO_3$, and $MgFeSiO_4$) and crystalline (forsterite and enstatite) silicate grains populating the disk surface. We find no evidence supporting the presence of troilite or fayalite (Section 2.3.1).
2. Given our model assumptions, we rule out a disk with a dust reservoir of $M_{\rm dust} \geqslant 10^{-6}\,M_\odot$, that is radially extended ($R_{\rm tap} \geqslant 100$ au) and externally irradiated with $\chi = 10^5$ (the FUV-integrated energy density relative to the solar neighborhood value). We find that such physical structure would be inconsistent with the available data (Section 3.1.1).
3. With the caveat that none of the currently available data are a probe for the disk mass, our model suggests a dust mass of $0.3\,M_\oplus$ and a gas mass of $6 \times 10^{-5}\,M_\odot$. The model also suggests an outer disk ($r > 10$ au) that is gas depleted. Our inferred dust and gas distributions are such that the gas-to-dust ratio is constant and equal to 1 for $r > 10$ au; constant and equal to 100 for $1 < r < 10$ au;

and variable, with an integrated value of 167, for $0.07 < r < 1$ au (Sections 3.1.1 and 3.1.2).

4. The external irradiation sets the disk FUV field beyond 10 au and stellar photons dominate the FUV field at shorter radii. Beyond 10 au, gas temperature reaches values above 1000 K—an order of magnitude higher than the characteristic temperatures expected in a nonirradiated disk with similar physical structure. Similarly, the effect of the external irradiation on molecular abundances is only noticeable beyond 10 au. In particular, for gas-phase water, we predict a 100-fold increase in abundance compared to a nonirradiated disk with the same physical structure (Section 3.2).

The unrivaled capabilities of JWST, combined with state-of-the-art numerical codes, enable us to present the first data-informed thermochemical model of an extremely irradiated disk at kiloparsec-distance scales. Our results imply that dust and gas material can be present within the first 10 au in a strongly irradiated disk. This supports the idea that planet formation is possible even in environments with extreme UV irradiation.

While the physical structure of XUE 1 aligns qualitatively with an external photoevaporation scenario, we cannot rule out model degeneracies that could allow for a larger, more massive disk under conditions of reduced external irradiation. Observing and characterizing a population of highly irradiated disks will help to break this degeneracy. A synergistic approach with other facilities, particularly at submillimeter wavelengths, is also needed to improve the characterization of the XUE 1 and other highly irradiated disks. This work serves as an initial foundation for such future efforts.

Acknowledgments

We are grateful to the anonymous referee for providing thoughtful and helpful comments that improved the manuscript. We thank Jayatee Kanwar and Sebastián Hernández for insightful discussions on modeling mid-IR spectroscopy, and Rebecca Zoshak for proofreading the manuscript. This project is supported by NASA STScI grant No. JWST-GO-01759.002-A. The Center for Exoplanets and Habitable Worlds is supported by the Pennsylvania State University and the Eberly College of Science. The research of T.P. was partly supported by the Deutsche Forschungsgemeinschaft (DFG, German Research Foundation) in the research unit "Transition Disks" (Ref no. 325594231 – FOR 2634/2 – TE 1024/2-1) and in the Excellence Cluster ORIGINS – EXC 2094 – 390783311. E.S. is supported by the international Gemini Observatory, a program of NSF NOIRLab, which is managed by the Association of Universities for Research in Astronomy (AURA) under a cooperative agreement with the U.S. National Science Foundation, on behalf of the Gemini partnership of Argentina, Brazil, Canada, Chile, the Republic of Korea, and the United States of America. T.J.H. acknowledges funding from a Royal Society Dorothy Hodgkin Fellowship and UKRI guaranteed funding for a Horizon Europe ERC consolidator grant (EP/Y024710/1). A.B. and J.F. acknowledge support from the Swedish National Space Agency (grant No. 2022-00154). M.C.R.T. acknowledges support by the German Aerospace Center (DLR) and the Federal Ministry for Economic Affairs and Energy (BMWi) through program 50OR2314, "Physics and Chemistry of Planet-forming disks in extreme environments." V.R. acknowledges the support of the European Union's Horizon 2020 research and innovation program and the European Research Council via the ERC Synergy Grant "ECOGAL" (project ID 855130). This research has made use of the SVO Filter Profile Service "Carlos Rodrigo," funded by MCIN/AEI/10.13039/501100011033/ through grant No. PID2020-112949GB-I00. Some/all of the data presented in this article were obtained from the Mikulski Archive for Space Telescopes (MAST) at the Space Telescope Science Institute. The specific observations analyzed can be accessed via doi:10.17909/6nwv-6f56.

Facility: JWST.

ORCID iDs

Bayron Portilla-Revelo https://orcid.org/0000-0002-6278-9006
Konstantin V. Getman https://orcid.org/0000-0002-6137-8280
María Claudia Ramírez-Tannus https://orcid.org/0000-0001-9698-4080
Thomas J. Haworth https://orcid.org/0000-0002-9593-7618
Rens Waters https://orcid.org/0000-0002-5462-9387
Arjan Bik https://orcid.org/0000-0001-8068-0891
Eric D. Feigelson https://orcid.org/0000-0002-5077-6734
Inga Kamp https://orcid.org/0000-0001-7455-5349
Sierk E. van Terwisga https://orcid.org/0000-0002-1284-5831
Jenny Frediani https://orcid.org/0009-0003-7663-5280
Thomas Henning https://orcid.org/0000-0002-1493-300X
Andrew J. Winter https://orcid.org/0000-0002-7501-9801
Veronica Roccatagliata https://orcid.org/0000-0002-4650-594X
Thomas Preibisch https://orcid.org/0000-0003-3130-7796
E. Sabbi https://orcid.org/0000-0003-2954-7643
Peter Zeidler https://orcid.org/0000-0002-6091-7924
Michael A. Kuhn https://orcid.org/0000-0002-0631-7514

References

Adams, F. C. 2010, ARA&A, 48, 47
Antonellini, S., Kamp, I., Riviere-Marichalar, P., et al. 2015, A&A, 582, A105
Arabhavi, A. M., Kamp, I., Henning, T., et al. 2024, Sci, 384, 1086
Armitage, P. J. 2020, Astrophysics of Planet Formation (2nd ed.; Cambridge: Cambridge Univ. Press)
Bally, J., Testi, L., Sargent, A., & Carlstrom, J. 1998, AJ, 116, 854
Banzatti, A., Pontoppidan, K. M., Carr, J. S., et al. 2023, ApJL, 957, L22
Berné, O., Habart, E., Peeters, E., et al. 2024, Sci, 383, 988
Berné, O., Martin-Drumel, M.-A., Schroetter, I., et al. 2023, Natur, 621, 56
Bisbas, T. G., Bell, T. A., Viti, S., Yates, J., & Barlow, M. J. 2012, MNRAS, 427, 2100
Bisbas, T. G., Haworth, T. J., Barlow, M. J., et al. 2015, MNRAS, 454, 2828
Bressan, A., Marigo, P., Girardi, L., et al. 2012, MNRAS, 427, 127
Brooke, J. S. A., Bernath, P. F., Western, C. M., et al. 2016, JQSRT, 168, 142
Broos, P. S., Getman, K. V., Povich, M. S., et al. 2013, ApJS, 209, 32
Cazzoletti, P., van Dishoeck, E. F., Visser, R., Facchini, S., & Bruderer, S. 2018, A&A, 609, A93
Chen, Y., Girardi, L., Bressan, A., et al. 2014, MNRAS, 444, 2525
Chiang, E. I., & Goldreich, P. 1997, ApJ, 490, 368
Clarke, C. J. 2007, MNRAS, 376, 1350
Coleman, G. A. L., & Haworth, T. J. 2022, MNRAS, 514, 2315
Decleir, M., Gordon, K. D., & Andrews, J. E. 2022, ApJ, 930, 15
Desch, S., & Miret-Roig, N. 2024, SSRv, 220, 76
Díaz-Berríos, J. K., Guzmán, V. V., Walsh, C., et al. 2024, ApJ, 969, 165
Doi, J. K., & Kataoka, A. 2023, ApJ, 957, 11
Draine, B. T. 1978, ApJS, 36, 595
Dubrulle, B., Morfill, G., & Sterzik, M. 1995, Icar, 114, 237
Dullemond, C. P., & Monnier, J. D. 2010, ARA&A, 48, 205
Eisner, J. A., Arce, H. G., Ballering, N. P., et al. 2018, ApJ, 860, 77
Ercolano, B., & Picogna, G. 2022, EPJP, 137, 1357

Facchini, S., Clarke, C. J., & Bisbas, T. G. 2016, MNRAS, 457, 3593
Fitzpatrick, E. L., Massa, D. , Gordon, K. D., Bohlin, R., & Clayton, G. C. 2019, ApJ, 886, 108
Fouesneau, M., Andrae, R., Dharmawardena, T., et al. 2022, A&A, 662, A125
Gasman, D., van Dishoeck, E. F., Grant, S. L., et al. 2023, A&A, 679, A117
Getman, K. V., & Feigelson, E. D. 2021, ApJ, 916, 32
Getman, K. V., Feigelson, E. D., Garmire, G. P., et al. 2022, ApJ, 935, 43
Goicoechea, J. R., Le Bourlot, J., Black, J. H., et al. 2024, A&A, 689, L4
Gordon, I. E., Rothman, L. S., Hargreaves, R. J., et al. 2022, JQSRT, 277, 107949
Gordon, K. D., Cartledge, S. , & Clayton, G. C. 2009, ApJ, 705, 1320
Gordon, K. D., Clayton, G. C., Decleir, M., et al. 2023, ApJ, 950, 86
Gordon, K. D., Misselt, K. A., Bouwman, J., et al. 2021, ApJ, 916, 33
Guidi, G., Isella, A., Testi, L., et al. 2022, A&A, 664, A137
Gullbring, E., Hartmann, L., Briceño, C., & Calvet, N. 1998, ApJ, 492, 323
Harries, T., Haworth, T., Acreman, D., Ali, A., & Douglas, T. 2019, A&C, 27, 63
Haworth, T. J., Clarke, C. J., Rahman, W., Winter, A. J., & Facchini, S. 2018, MNRAS, 481, 452
Haworth, T. J., Coleman, G. A. L., Qiao, L., Sellek, A. D., & Askari, K. 2023, MNRAS, 526, 4315
Henney, W. J., & O'Dell, C. R. 1999, AJ, 118, 2350
Henning, T., Kamp, I., Samland, M., et al. 2024, PASP, 136, 054302
Huang, S., Portegies Zwart, S., & Wilhelm, M. J. C. 2024, A&A, 689, A338
Hughes, A. M., Wilner, D. J., Qi, C., & Hogerheijde, M. R. 2008, ApJ, 678, 1119
Jang, H., Waters, R., Kaeufer, T., et al. 2024, A&A, 691, 148
Johnstone, D., Hollenbach, D., & Bally, J. 1998, ApJ, 499, 758
Kaeufer, T., Min, M., Woitke, P., Kamp, I., & Arabhavi, A. M. 2024, A&A, 687, A209
Kaeufer, T., Woitke, P., Min, M., Kamp, I., & Pinte, C. 2023, A&A, 672, A30
Kamp, I. 2015, in EJP Web of Conf. 102, Summer School "Protoplanetary Disks: Theory and Modeling Meet Observations", ed. I. Kamp, P. Woitke, & J. D. Ilee (Les Ulis: EDP Sciences), 00013
Kamp, I., Galli, D., & Rab, C. 2024, in Astrochemical Modeling: Practical Aspects of Microphysics in Numerical Simulations, ed. S. Bovino & T. Grassi (Amsterdam: Elsevier), 283
Kamp, I., Henning, T., Arabhavi, A. M., et al. 2023, FaDi, 245, 112
Kamp, I., Thi, W. F., Woitke, P., et al. 2017, A&A, 607, A41
Kamp, I., Tilling, I., Woitke, P., Thi, W. F., & Hogerheijde, M. 2010, A&A, 510, A18
Keppler, M., Benisty, M., Müller, A., et al. 2018, A&A, 617, A44
Keyte, L., & Haworth, T. J. 2025, MNRAS, 537, 598
King, R. R., Naylor, T., Broos, P. S., Getman, K. V., & Feigelson, E. D. 2013, ApJS, 209, 28
Kóspál, Á., Ábrahám, P., Diehl, L., et al. 2023, ApJL, 945, L7
Krumholz, M. R., McKee, C. F., & Bland-Hawthorn, J. 2019, ARA&A, 57, 227
Kuffmeier, M., Jensen, S. S., & Haugbølle, T. 2023, EPJP, 138, 272
Law, D. R., E. Morrison, J., Argyriou, I., et al. 2023, AJ, 166, 45
Lin, C.-L., Ip, W.-H., Hsiao, Y., et al. 2023, AJ, 166, 82
Lynden-Bell, D., & Pringle, J. E. 1974, MNRAS, 168, 603
Macías, E., Guerra-Alvarado, O., Carrasco-González, C., et al. 2021, A&A, 648, A33
Manara, C. F., Ansdell, M., Rosotti, G. P., et al. 2023, in ASP Conf. Ser. 534, Protostars and Planets VII, ed. S. Inutsuka et al. (San Francisco, CA: ASP), 539
Massi, F., Giannetti, A., Di Carlo, E., et al. 2015, A&A, 573, A95
Mathis, J. S., Rumpl, W., & Nordsieck, K. H. 1977, ApJ, 217, 425
McElroy, D., Walsh, C., Markwick, A. J., et al. 2013, A&A, 550, A36
Min, M., Hovenier, J. W., & de Koter, A. 2005, A&A, 432, 909
Mordasini, C., Alibert, Y., Benz, W., Klahr, H., & Henning, T. 2012, A&A, 541, A97
O'Dell, C. R., Wen, Z., & Hu, X. 1993, ApJ, 410, 696
Offer, A. R., van Hemert, M. C., & van Dishoeck, E. F. 1994, JChPh, 100, 362
Padoan, P., Kritsuk, A., Norman, M. L., & Nordlund, Å. 2005, ApJL, 622, L61
Panić, O., Haworth, T. J., Petr-Gotzens, M. G., et al. 2021, MNRAS, 501, 4317
Perotti, G., Christiaens, V., Henning, T., et al. 2023, Natur, 620, 516
Pontoppidan, K. M., Salyk, C., Banzatti, A., et al. 2024, ApJ, 963, 158
Portilla-Revelo, B., Kamp, I., Rab, C., et al. 2022, A&A, 658, A89
Povich, M. S., Kuhn, M. A., Getman, K. V., et al. 2013, ApJS, 209, 31
Preibisch, T., Kim, Y.-C., Favata, F., et al. 2005, ApJS, 160, 401
Qiao, L., Coleman, G. A. L., & Haworth, T. J. 2023, MNRAS, 522, 1939
Qiao, L., Haworth, T. J., Sellek, A. D., & Ali, A. A. 2022, MNRAS, 512, 3788
Rab, C., Güdel, M., Woitke, P., et al. 2018, A&A, 609, A91
Rahmann, U., Kreutner, W., & Kohse-Höinghaus, K. 1999, ApPhB, 69, 61
Ramirez-Tannus, M. C., Backs, F., Bik, A., et al. 2021, Physics and Chemistry of Planet-Forming Disks in Extreme Radiation Environments, JWST Proposal. Cycle 1, ID., #1759
Ramírez-Tannus, M. C., Poorta, J., Bik, A., et al. 2020, A&A, 633, A155
Ramírez-Tannus, M. C., Bik, A., Cuijpers, L., et al. 2023, ApJL, 958, L30
Richert, A. J. W., Feigelson, E. D., Getman, K. V., & Kuhn, M. A. 2015, ApJ, 811, 10
Richert, A. J. W., Getman, K. V., Feigelson, E. D., et al. 2018, MNRAS, 477, 5191
Roccatagliata, V., Bouwman, J., Henning, T., et al. 2011, ApJ, 733, 113
Rodrigo, C., & Solano, E. 2020, XIV.0 Scientific Meeting (virtual) of the Spanish Astronomical Society, 182
Rodrigo, C., Solano, E., & Bayo, A. 2012, SVO Filter Profile Service Version 1.0, IVOA Working Draft 15 October 2012, doi:10.5479/ADS/bib/2012ivoa.rept.1015R
Russeil, D., Adami, C., Bouret, J. C., et al. 2017, A&A, 607, A86
Russeil, D., Zavagno, A., Motte, F., et al. 2010, A&A, 515, A55
Schöier, F. L., van der Tak, F. F. S., van Dishoeck, E. F., & Black, J. H. 2005, A&A, 432, 369
Schwarz, K. R., & Bergin, E. A. 2014, ApJ, 797, 113
Sellek, A. D., Booth, R. A., & Clarke, C. J. 2020, MNRAS, 492, 1279
Shakura, N. I., & Sunyaev, R. A. 1973, A&A, 24, 337
Tabone, B., van Hemert, M. C., van Dishoeck, E. F., & Black, J. H. 2021, A&A, 650, A192
Telleschi, A., Güdel, M., Briggs, K. R., Audard, M., & Palla, F. 2007, A&A, 468, 425
Thi, W. F., Kamp, I., Woitke, P., et al. 2013, A&A, 551, A49
Thi, W. F., Woitke, P., & Kamp, I. 2011, MNRAS, 412, 711
Townsley, L. K., Broos, P. S., Garmire, G. P., & Povich, M. S. 2019, ApJS, 244, 28
Tripathi, A., Andrews, S. M., Birnstiel, T., & Wilner, D. J. 2017, ApJ, 845, 44
Tychoniec, Ł., Tobin, J. J., Karska, A., et al. 2018, ApJS, 238, 19
van Boekel, R., Min, M., Waters, L. B. F. M., et al. 2005, A&A, 437, 189
van der Tak, F. F. S., Lique, F., Faure, A., Black, J. H., & van Dishoeck, E. F. 2020, Atoms, 8, 15
van Terwisga, S. E., & Hacar, A. 2023, A&A, 673, L2
van Terwisga, S. E., Hacar, A., & van Dishoeck, E. F. 2019, A&A, 628, A85
van Terwisga, S. E., Hacar, A., van Dishoeck, E. F., Oonk, R., & Portegies Zwart, S. 2022, A&A, 661, A53
Vincke, K., & Pfalzner, S. 2018, ApJ, 868, 1
Walborn, N. R. 2003, in IAU Symp. 212, A Massive Star Odyssey: From Main Sequence to Supernova, ed. K. van der Hucht, A. Herrero, & C. Esteban (Cambridge: Cambridge Univ. Press), 13
Walsh, C., Millar, T. J., & Nomura, H. 2013, ApJL, 766, L23
Wilhelm, M. J. C., Portegies Zwart, S., Cournoyer-Cloutier, C., et al. 2023, MNRAS, 520, 5331
Williams, J. P. 2021, Introduction to the Interstellar Medium (Cambridge: Cambridge Univ. Press)
Winter, A. J., Benisty, M., Manara, C. F., & Gupta, A. 2024, A&A, 691, A169
Winter, A. J., & Haworth, T. J. 2022, EPJP, 137, 1132
Woitke, P. 2015, in EPJ Web of Conf. 102, Summer School "Protoplanetary Disks: Theory and Modeling Meet Observations", ed. I Kamo, P. Woitke, & J. D. Ilee (Les Ulis: EDP Sciences), 00007
Woitke, P., Kamp, I., & Thi, W. F. 2009, A&A, 501, 383
Woitke, P., Kamp, I., Antonellini, S., et al. 2019, PASP, 131, 064301
Woitke, P., Min, M., Pinte, C., et al. 2016, A&A, 586, A103
Woitke, P., Thi, W. F., Arabhavi, A. M., et al. 2024, A&A, 683, A219
Zannese, M., Tabone, B., Habart, E., et al. 2024, NatAs, 8, 577
Zannese, M., Tabone, B., Habart, E., et al. 2025, A&A, 696, A99
Zhu, H., Tian, W., Li, A., & Zhang, M. 2017, MNRAS, 471, 3494